FINITE-VOLUME DISCRETIZATION FOR THE DEFORMATION OF FRACTURED MEDIA

Eren Ucar[a], Eirik Keilegavlen[a], Inga Berre[a,b], Jan Martin Nordbotten[a,c]

[a] Department of Mathematics, University of Bergen, Bergen, Norway

[b] Christian Michelsen Research, Bergen, Norway

[c] Department of Civil and Environmental Engineering, Princeton University, Princeton, NJ, USA

Corresponding author: Eren Ucar, email: eren.ucar@uib.no

ABSTRACT

Simulating the deformation of fractured media requires the coupling of different models for the deformation of fractures and the formation surrounding them. Motivated by its applicability to coupled flow and mechanical deformation in porous media, we propose a method for calculating the deformation that is constructed using a cell-centred finite-volume approximation, in particular from the family of multi-point stress approximations (MPSA). By coupling the deformation of pre-existing fractures with that of the surrounding domain through internal boundary conditions, the existing MPSA methods are extended to include models with fractures. This approach is natural within the finite-volume framework, since tractions are defined on surfaces of the grid. We consider the fracture surfaces as line pairs for 2D (faces for 3D) studies, which displace relative to each other. The method is capable of modelling open and closed fractures with complex and nonlinear relationships governing the displacements and tractions at the fracture surfaces. We validate our proposed approach using both problems for which analytical solutions are available and more complex benchmark problems, including comparison with a finite-element discretization.

1. INTRODUCTION

Subsurface rock is a porous medium containing fluids under complex in situ stress conditions [1,2]. Advances in the understanding of fluid flow and rock mechanics have vital importance in the development of several subsurface applications, including exploitation of geothermal-energy systems [3], enhanced recovery from oil and gas reservoirs [4], CO_2 storage [4,5] and underground storage of natural gas [6]. Deformation of the subsurface due to engineering operations or natural processes involves slit-like discontinuities (such as fractures) because of the constitution of subsurface rock. In many situations, these structures will dominate the mechanical behaviour; thus, the feasible modelling of rock mechanics for subsurface applications requires effective incorporation of fractures. The objective of this work is to describe and implement a numerical method to model mechanical deformations in fractured formations. Such a model is expected to be an important contribution to efficient hydromechanical coupling, particularly for subsurface applications.

In the literature on the computational analysis of fractured domains, two main approaches have been applied: the boundary-element method (BEM) and the finite-element method (FEM) [7,8]. The BEM has been effectively applied to fracture problems for the past several decades, and its area of application has recently widened [3,9-13].

The BEM can accommodate problems including nonhomogeneous materials using Green's functions [9] and can be extended to 3D simulations [14]. Alternatively, one could also choose to discretize the linear elasticity equations via FEM; in this case, the method must be 'enhanced' to accommodate discontinuous deformations [15]. In FEM simulations, classical approaches to incorporating fractures into the model are Lagrange multipliers [16,17], the penalty method [18], and the augmented Lagrangian method. However, questions still arise for problems that include multi-physics modelling, such as that of flow and mechanical deformations. Strategies for coupling the flow and mechanical deformations have been analysed and applied for several problems [10,19-21]. In most studies, the flow equations are generally discretized by conservative schemes such as the finite-volume method (FVM), whereas the mechanical equations are approximated by the FEM or BEM. The coupling of different numerical methods may not be advantageous due to different data structures of the disparate schemes. Moreover, it is also common to use two different software packages to solve the coupled problem, which requires an additional iteration procedure.

An alternative that avoids these difficulties is to discretize the full poro-mechanical system with the FVM. Specifically, we consider a cell-centred FVM for elastic deformation in porous media as a counterpart to finite-volume flow calculations in porous media [22]. The method is called the multi-point stress approximation (MPSA) due to its similar data structure to multi-point flux approximation (MPFA) methods, which have been developed in the context of flow problems. The applicability of the MPSA method to the coupled flow and mechanics problem is already discussed elsewhere [23]. Recently, the capabilities of MPSA have been widely extended by imposing weak transpose conditions on the discretization [24]. In addition to its capability for solving multi-physics problems, two features of MPSA in particular allow the efficient inclusion of fractures. First, MPSA represents the mean solution within the grid cell; therefore, it does not explicitly imply a spatially continuous approximation. Further, MPSA leads to explicit expressions for traction forces at the grid faces. In the following sections, we will explain how fracture discretization exploits these features in detail. As MPSA has been described elsewhere [22-24], we will concentrate only on the numerical modelling of problems that include fractured formations. The focus of this study is to describe the incorporation of fractures into the MPSA approach for both 2D and 3D studies and to discuss its convergence properties for the cases in which the numerical system includes fractures.

With the goal of developing a numerical method with a broad application area, the method is extended to cover a wide range of mechanical problems in fractured media. We concentrate on three main modelling problems: (1) fracture deformation defined by prescribed displacements on fractures, (2) slip due to the applied tractions at the fracture surfaces and (3) displacements controlled by friction between fracture surfaces. It should be noted that the propagation and initiation mechanisms of fractures are outside the scope of this study.

The study is structured as follows. The model equations and the inclusion of fractures are presented in Section 2. Section 3 starts with the description of the grid structure for the method, followed by the explanation of the numerical discretization and algorithms. We validate our approach in Section 4 by conducting comparison studies between MPSA and analytical solutions existing in the literature. In addition, a numerical

experiment including a complicated fracture network and a 3D example are also presented. Finally, we present our conclusions.

2. GOVERNING EQUATIONS

We model the intact rock in the subsurface using the approximation of linearized elasticity, as it is the most commonly used model for the deformation of rock [1]. Therefore, we start with the presentation of equations with linear momentum balance. However, linear elasticity may not be sufficient to model all aspects of deformation for subsurface structures. It is well known that slit-like discontinuities, such as cracks or fractures, are a common type of defect in geological rock [1]. Fractures divide a rock mass into different parts and can be subject to different governing equations related to the application area. An idealized fracture has two planar surfaces, and the surfaces may or may not be in contact with each other. Accordingly, the presentation of the governing equations will correspond to the different types of physical relations for fracture faces. Since the equations are correlated with the surfaces of fracture faces, it is natural to model fracture faces as internal boundary conditions in the domain and to construct the governing relations between the fracture faces. Here, we explain this concept with equations in detail.

2.1. Linear Momentum Balance

Let Ω be a d-dimensional domain (d=2 or 3), and let us consider the static momentum-balance problem for an elastic medium. The problem is defined by the following equations:

$$\int_{\partial\Omega} \boldsymbol{T}(\boldsymbol{n})dA + \int_{\Omega} \boldsymbol{f}dV = 0 \ on \ \Omega, \tag{1}$$

$$\boldsymbol{u} = \boldsymbol{u}^D \ on \ \partial\Omega^D,$$

$$\boldsymbol{T}(\boldsymbol{n}) = \boldsymbol{T}^N \ on \ \partial\Omega^N.$$

Here, $\boldsymbol{T}(\boldsymbol{n})$ are the forces on the surfaces of Ω, identified by the outward normal vector $\boldsymbol{n}$, $\boldsymbol{f}$ are body forces acting on the material, and $\boldsymbol{u}$ is the unknown displacement field. D and N are the two exponents denoting Dirichlet and Neumann boundary conditions, respectively. In infinitesimal strain theory, the surface forces can be expressed as

$$\boldsymbol{T}(\boldsymbol{n}) = \boldsymbol{\sigma} \cdot \boldsymbol{n}, \tag{2}$$

where $\boldsymbol{\sigma}$ is the Cauchy stress tensor and $\boldsymbol{\varepsilon}$ is the symmetric part of the deformation gradient $\boldsymbol{\varepsilon} = (\nabla\boldsymbol{u} + (\nabla\boldsymbol{u})^T)/2$. For a general material, the Cauchy stress tensor can be related to strain through Hooke's Law,

$$\boldsymbol{\sigma} = \mathbb{C}:\boldsymbol{\varepsilon}, \tag{3}$$

where $\mathbb{C}$ is the stiffness tensor, which can be expressed by Lamé parameters μ and λ for an isotropic medium. The Cauchy stress tensor can be rewritten in terms of Lamé parameters as

$$\mathbb{C}:\boldsymbol{\varepsilon} = 2\mu\boldsymbol{\varepsilon} + \lambda \ tr(\boldsymbol{\varepsilon})\boldsymbol{I}. \tag{4}$$

2.2. Fractures as Internal Boundaries

We are interested in a problem in which the domain has internal boundaries, Γ, that can be considered as discontinuities, i.e., fracture surfaces. Motivated by the method of

'split nodes' presented by [25], the fracture surfaces are considered as line pairs for 2D (faces for 3D) studies, which displace relative to one another, as illustrated in Fig. 1. Following the notation for fracture surfaces from, for example, [12,16], we denote the two sides of the discontinuities by subscripts + and -. The tractions on the fracture surfaces are defined separately for each + and - surface. Because of continuity and equilibrium conditions, the relation between traction forces can be written as

$$T_+^\Gamma = T_-^\Gamma, \tag{5}$$

where T_+^Γ and T_-^Γ are the traction forces on the positive- and negative-side fracture surfaces. Equation 5 holds when the tractions are approximated using infinitesimal strains.

In addition to equilibrium conditions between forces on fracture surfaces (Eq. 5), one more relation for fracture faces is required to complete the system of equations. The presented method can be constructed to include any type of fracture constitutive model for fracture surfaces. In the modelling of subsurface applications, there are three common types of problems one may need to solve. Here, we focus on and describe these problems in separate subsections.

2.2.1. Defined Displacement Jump at the Fracture Surfaces

Fracture behaviour can be modelled by a constitutive model that defines a jump between + and – surfaces. As an example motivated by subsurface applications, Rahman et al. [26] considered a joint-deformation model that predicts a displacement jump according to the injection pressure to model hydraulic stimulation in enhanced geothermal systems. One may need to calculate stress alteration in the system due to the displacement jump accordingly. The prescribed jump between the + and – surfaces can be written as

$$[\![u]\!] = \left(u_+^\Gamma - u_-^\Gamma \right) \, on \, \Gamma^d. \tag{6}$$

Here, Γ^d is the part of the internal boundary whereon prescribed displacements jumps, $[\![u]\!]$, are applied, and u_+^Γ and u_-^Γ are the displacements on the positive and negative sides of the fracture surfaces, respectively.

2.2.2. Defined Traction at the Fracture Surfaces

Having considered the problems with displacement jumps between fracture surfaces in the previous subsection, it is also reasonable to examine the problems that include unknown displacement-jump distributions along the fracture. To define the problem properly, the distribution of traction applied to the fracture surfaces should be known. A pressurized fracture network in an elastic medium can be considered as an example since applied pressure acts as a normal traction at the fracture surfaces. The defined traction forces at the fracture surfaces can be written as
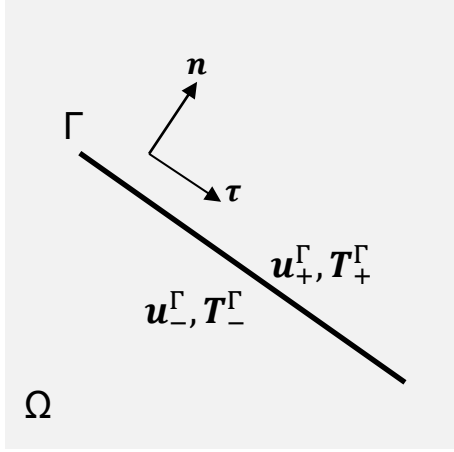
$$T(n) = T^\Gamma \, on \, \Gamma^T. \tag{7}$$

Here, Γ^T is the part of the internal boundary whereon prescribed tractions, T^Γ, are applied.

2.2.3. Fractures Controlled by a Friction Model

In addition to the problem types described in subsections 2.2.1 and 2.2.2, another common type of problem may be considered. A friction law can control the fracture displacements in the considered domain. The friction law determines the shear stress on the fracture and is generally motivated by laboratory experiments [27]. The simplest example of a friction model includes constant friction as

4

$$T_\tau^\Gamma = \mu_f T_n^\Gamma, \tag{8}$$

using the local coordinate system for a fracture shown in Fig. 1. Here, T_τ^Γ and T_n^Γ are the magnitudes of the shear and normal tractions on the fracture, respectively, and μ_f is the contact friction between the fracture surfaces.

Fig. 1 Modelling of a fracture. Fractures are modelled as internal boundaries having two sides, labelled + and -.

The fracture constitutive model, which includes friction, is only valid when the fracture surfaces are in contact with each other. Following the Kuhn-Tucker conditions of contact mechanics [28], when the fracture is under compression, we disallow the penetration of fracture surfaces. The modelling of this problem requires a more elaborate approach because of the nonlinearity caused by Eq. 8, which relates the magnitudes of the tractions. Moreover, the model requires a definition for the friction coefficient between surfaces. There are numerous studies related to modelling the friction coefficient. The most common friction models are static friction, linear slip-weakening [29], linear time-weakening [30], and Dieterich-Ruina rate-state friction with an aging law [31]. Since the analysis of different friction models is outside the scope of the current study, we use a static friction value throughout our simulations; however, the modelling framework applies to more complex friction coefficients as well.

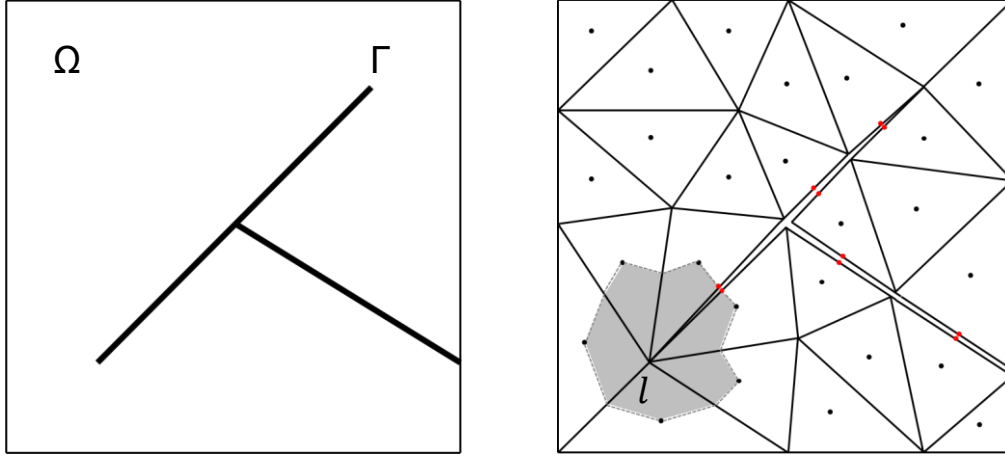## 3. THE DISCRETIZATION OF MPSA WITH FRACTURES

In this section, we first introduce the grid structure that is necessary to discretize the system of equations given in the previous section. Although we discretize three different types of governing equations for the fractures, described in Sections 2.2, the grid structure is the same for all types of problems. The section continues with the brief introduction of MPSA, where we present the discrete form of the momentum-conservation equation along with the discrete forms of the surface stress and the displacement. Moreover, we discuss how to create the discrete system of equations for each type of problem that we consider.

3.1. Grid Structure

The simulation domain Ω is discretized by a set of control volumes Ω_i. For cells i and j sharing a boundary, the shared boundary is denoted as $\omega_{i,j}$. The set of faces of the grid is denoted by $\mathcal{F}$, while the set of faces on the boundary of a cell is denoted by $\mathcal{F}_{\Omega_i}$. To

construct the MPSA discretization, the cells are further divided into sub-cells so that each face is split into two sub-faces for 2D studies and three sub-faces for 3D studies. The volume associated with corner l and cell i is termed a sub-cell and denoted as $\widetilde{\Omega}_{i,l}$. We will refer to the sub-faces as $\widetilde{\omega}_{i,j,l}$, where l is the cell corner associated with the sub-face.

Among the set of faces of the grid $\mathcal{F}$, there may be ordinary internal faces, internal boundary faces, and external boundary faces. We consider the internal boundary faces as the faces of the fractures. To impose fracture relations, such as those defined in Eqs. 5-8, we must represent the displacement on both sides of the fracture. Thus, we create a mesh that includes face pairs corresponding to each face of the fracture. The fractures that have immersed tips (edges for 3D), i.e., the fractures that do not reach the edge of the domain, are treated carefully. The vertices that correspond to the immersed tips of the fractures combine the two faces of the fractures. This approach naturally forces the magnitude of the slip to zero at the vertices corresponding to the immersed tips of the fractures. Figure 2 shows a conceptual domain, including the fractures and the mesh of the domain.

Fig. 2 Conceptual domain including fractures (left). Two-dimensional conceptual illustration of the grid structure, where the fractures are explicitly represented (right). Black dots represent the unknown locations of cell centres, while red dots represent the unknown locations of fracture faces. (Sub-cells creating an interaction region are shown as shaded regions.)

3.2. Multi-Point Stress Approximation

Considering the grid structure explained above, the momentum conservation for each cell Ω_i can be written as

$$-\int_{\Omega_i} \boldsymbol{f} dV = \int_{\partial\Omega_i} \boldsymbol{T}(\boldsymbol{n}) dA = \sum_j \int_{\omega_{i,j}} \boldsymbol{T}(\boldsymbol{n}) dA. \tag{9}$$

Furthermore, by introducing the surface stresses between cells i and j, $\boldsymbol{T}_{i,j}$, as the surface-averaged stress over face $\omega_{i,j}$, Eq. 9 can be rewritten as

$$-\boldsymbol{f}_i = \frac{1}{|\Omega_i|} \sum_j |\omega_{i,j}| \boldsymbol{T}_{i,j}, \tag{10}$$

where $-\boldsymbol{f}_i$ is the volume-averaged force over cell Ω_i.

MPSA methods are constructed by expressing the surface stress between cell i and j, $\boldsymbol{T}_{\mathrm{i},j}$, as a linear function of the cell-centre displacements $\boldsymbol{u}_i$, such that

$$\boldsymbol{T}_{\mathrm{i},j} = \sum_k t_{i,j,l,k}\boldsymbol{u}_k, \tag{11}$$

where $t_{i,j,l,k}$ is the stress-weight tensor and k denotes the cells that are neighbours to face $\omega_{i,j}$ and associated with corner l. MPSA methods can be divided into several categories according to the location of the considered neighbours (i.e., interaction regions) for face $\omega_{i,j}$ during the calculation of stress-weight tensors. On the right side of Fig. 2, the interaction region consisting of all sub-faces and all sub-cells adjacent to corner l is shown as the shaded area. Recently, a new type of MPSA method, termed MPSA-W, was developed with the motivation of seeking improved convergence properties for simplex grids. MPSA-W enforces symmetry in a weak sense on the stress tensor by altering the definition of the transpose term, which results in superior properties, as discussed in [24]. MPSA-W is robust on both simplex and Cartesian grids, and it has a lower computational cost than the MPSA-O methods [24].

Regardless of the type of MPSA, discretization starts with a linear approximation for displacement within each sub-cell $\widetilde{\Omega}_{i,l}$:

$$\boldsymbol{u} \approx \boldsymbol{u}_i + \boldsymbol{G}_{i,l} \cdot (\boldsymbol{x} - \boldsymbol{x}_i), \tag{12}$$

where $\boldsymbol{u}_i$ is the cell-centre displacement, $\boldsymbol{x}_i$ is the cell-centre and $\boldsymbol{G}_{i,l}$ is the gradient associated with corner l and cell i. Eq. 12 shows the basis functions created on each sub-cell. The two variables in Eq. 12, the gradients, $\boldsymbol{G}_{i,l}$, and cell-centre displacements, $\boldsymbol{u}_i$, define the discrete displacements in the domain.

Following [24], the rest of the discretization of the problem is divided into two parts for the sake of simplicity. First, a local linear system is created for each vertex of the domain, and gradients are eliminated by solving the local systems. Then, the global discretization in terms of cell-centre displacements is obtained. In the following sections, we show how the internal boundaries affect the local and global systems.

3.3. Construction of the Local Linear System without Fractures

As a foundation, we start with the construction of the local systems without fractures. To create a local linear system at each vertex of the domain, two continuity conditions are imposed on each sub-face. First, the continuity of stress over a sub-face is written as

$$\left[\mathbb{C}_i : \boldsymbol{G}_{i,l} + \langle \mathbb{C}_i : \boldsymbol{G}_{i,l} \rangle^T\right] \cdot \overline{\boldsymbol{n}}_{i,j,l} - \left[\mathbb{C}_j : \boldsymbol{G}_{j,l} + \langle \mathbb{C}_j : \boldsymbol{G}_{j,l} \rangle^T\right] \cdot \overline{\boldsymbol{n}}_{i,j,l} = 0, \tag{13}$$

where $\overline{\boldsymbol{n}}_{i,j,l}$ is the average normal vector for sub-face $\widetilde{\omega}_{i,j,l}$. The details of the calculation of the weak transpose term, $\langle \mathbb{C}_j : \boldsymbol{G}_{j,l} \rangle^T$, can be found in [24].

Similarly, the continuity of displacement over a sub-face can be written as

$$\boldsymbol{u}_i + \boldsymbol{G}_{i,l}(\widetilde{\boldsymbol{x}}_{i,m,l} - \boldsymbol{x}_i) - \boldsymbol{u}_j + \boldsymbol{G}_{j,l}(\widetilde{\boldsymbol{x}}_{i,m,l} - \boldsymbol{x}_j) = 0, \tag{14}$$

where $\widetilde{\boldsymbol{x}}_{i,m,l}$ is the calculated continuity point, located one-third of the distance from the face centre to the considered corner, as suggested in [24]. Finally, combining Eq. 13 and 14, the linear system for each vertex in the grid can be expressed as follows:

$$\begin{pmatrix} \boldsymbol{n}^T \mathbb{C} & 0 \\ \boldsymbol{D}_G & \boldsymbol{I} \\ 0 & \boldsymbol{I} \end{pmatrix}\begin{pmatrix} \boldsymbol{G} \\ \boldsymbol{U} \end{pmatrix} = \begin{pmatrix} \boldsymbol{0} \\ \boldsymbol{0} \\ \boldsymbol{I} \end{pmatrix}, \tag{15}$$

where $\boldsymbol{D}_G$ contains distances from the cell centres to continuity points, $\boldsymbol{G}$ represents gradients associated with the interaction region, $\boldsymbol{U}$ represents the cell-centre

displacements, and $\boldsymbol{I}$ is the identity matrix. The local linear system is constructed such that a unit displacement in one cell centre at a time is forced. After the local system is solved for $\boldsymbol{G}$, the gradients can be inserted into Eq. 11 to obtain the desired expressions for surface forces on a sub-face in terms of cell-centre displacements.

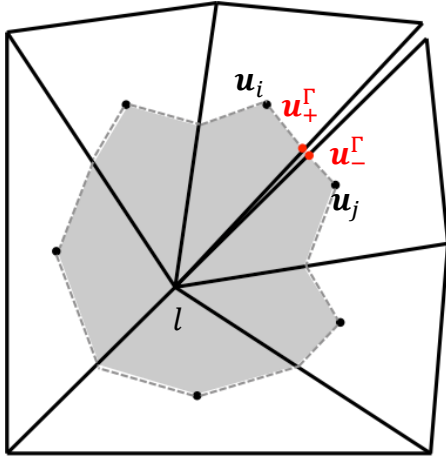### 3.4. Fracture Implementation in the Local Linear System
We now focus on a local system that includes internal boundary conditions corresponding to the situation illustrated in Fig. 3. As explained in Section 3.1, the unknowns representing the fracture surfaces are located at the face centres. For cells i and j, which contain fracture faces in between, the displacements at the fracture faces can be calculated as

$$\boldsymbol{u}_+^\ulcorner = \boldsymbol{u}_i + \boldsymbol{G}_{i,l}\big(\widetilde{\boldsymbol{x}}_{i,m,l} - \boldsymbol{x}_i\big), \tag{16}$$
$$\boldsymbol{u}_-^\ulcorner = \boldsymbol{u}_j + \boldsymbol{G}_{j,l}\big(\widetilde{\boldsymbol{x}}_{i,m,l} - \boldsymbol{x}_j\big),$$

where $\widetilde{\boldsymbol{x}}_{i,m,l}$ is the continuity point on sub-face $\widetilde{\omega}_{i,m,l}$. If we include Eq. 16 in the former local linear system, Eq. 15, the new local system becomes

$$\begin{pmatrix} \boldsymbol{n}^T\mathbb{C} & 0 & 0 \\ \boldsymbol{D}_G & \boldsymbol{I} & 0 \\ \boldsymbol{D}_G^\ulcorner & \boldsymbol{I} & -\boldsymbol{I} \\ 0 & \boldsymbol{I} & 0 \\ 0 & 0 & \boldsymbol{I} \end{pmatrix} \begin{pmatrix} \boldsymbol{G} \\ \boldsymbol{U} \\ \boldsymbol{U}^\ulcorner \end{pmatrix} = \begin{pmatrix} \boldsymbol{0} \\ \boldsymbol{0} \\ \boldsymbol{0} \\ \boldsymbol{I} \\ \boldsymbol{I} \end{pmatrix}, \tag{17}$$

where $\boldsymbol{D}_G^\ulcorner$ contains distances from the centres of the cells that have internal boundaries to the continuity points. $\boldsymbol{U}^\ulcorner$ represents both the + and – displacements at the fracture faces. By solving Eq. 17, we can obtain the displacement gradients in terms of both cell-centre displacements and the displacements defined at the fracture faces.

Fig. 3 Fracture implementation in the local linear system

3.5. Construction of the Global Linear System
By solving the local systems for each vertex in the grid, the discrete tractions can be obtained in the desired form of Eq. 11. Furthermore, the balance equation for each cell Ω_i can be written accordingly. The final form of the force-balance equation in terms of displacements can be written as

$$-\boldsymbol{f}_i = \frac{1}{|\Omega_i|}\sum_j |\omega_{i,j}|\boldsymbol{T}_{i,j} = \frac{1}{|\Omega_i|}\sum_j |\omega_{i,j}|\sum_k t_{i,j,l,k}\boldsymbol{u}_k. \tag{18}$$

The final global linear system is constructed by combining the balance equations for all cells. Introducing L and R as matrices corresponding to the relations between fracture surfaces, Eq. 18 can be written in the form of

$$\underbrace{\begin{pmatrix} \psi^{\Omega} & \psi_{+}^{\Gamma} & \psi_{-}^{\Gamma} \\ \tilde{t}^{\Omega} & \tilde{t}_{+}^{\Gamma} & \tilde{t}_{-}^{\Gamma} \\ & L & \end{pmatrix}}_{} \begin{pmatrix} U \\ U_{+}^{\Gamma} \\ U_{-}^{\Gamma} \end{pmatrix} = \begin{pmatrix} 0 \\ 0 \\ R \end{pmatrix} \qquad (19)$$

for a system that includes fractures. Here, the terms with superscript Ω are associated with the cell centres, while superscript Γ represents the terms associated with internal boundary conditions. Likewise, the subscripts + and – denote terms associated with the + and – sides of a fracture-face pair, respectively. The parameter ψ represents the terms of the force balance-equations in the form $\frac{1}{|\Omega_i|}\sum_j |\omega_{i,j}| \sum_k t_{i,j,l,k}$ (see Eq. 18), and $\tilde{t}$ represents the terms of the surface-stress definitions (see Eq. 11) in the form of $\left(\sum_k t_{i,j,l,k_+} - \sum_k t_{i,j,l,k_-}\right)$ as the difference of the surface stresses of the + and - faces. The first row in Eq. 19 is the force-balance equations for each cell in the grid, namely, Eq. 18. The second row represents the continuity of the stresses (Eq. 5) between each side of the fracture faces (+,-). The L and R matrices can be constructed differently according to the fracture problem that one would like to solve. In this paper, we will show how to create L and R matrices for only the three most common problems: defined displacement jump between fracture faces (Eq. 6), prescribed traction at the fracture faces (Eq. 7), and modelling of friction-controlled fractures (Eq. 8).

3.5.1. Defined Displacement Jump at the Fracture Surfaces

In this case, the fracture surfaces are modelled such that the surfaces are displaced relative to each other by a constant amount, $[\![u]\!]$, as in Eq. 6. The relative displacement $[\![u]\!]$ can also be considered an arbitrary distribution along parts of the fracture or the entire fracture. The L and R matrices in the Eq. 19 should be written as

$$L = (0 \quad I \quad -I), R = [\![u]\!]. \qquad (20)$$

It can be deduced from Eq. 20 that when $[\![u]\!]$ is equal to 0, the system disregards the existence of fractures.

3.5.2. Defined Traction at the Fracture Surfaces

Similarly, one would like to approximate the displacement distribution in the domain when stress is applied to the fracture surfaces. This approximation can be accomplished by creating the L and R matrices such that

$$L = (\tilde{\gamma}^{\Omega} \quad \tilde{\gamma}_{+}^{\Gamma} \quad \tilde{\gamma}_{-}^{\Gamma}), R = (T^{\Gamma}). \qquad (21)$$

Here, $\tilde{\gamma}$ represents the terms of the surface-stress definitions (see Eq. 11) in the form of $\left(\sum_k t_{i,j,l,k}\right)$ because the surface stresses at the fracture surfaces, T^{Γ}, are explicitly defined in this problem.

3.5.3. Fractures Controlled by a Friction Model

In addition to the problems discretized previously (with defined jump or traction at the fracture surfaces), a constitutive friction model may control the tractions of the fracture surfaces. In this problem, it is assumed that the shear stress is controlled through Eq. 8. If we assume that a constant friction, μ_f, controls the deformation behaviour of the fracture, the corresponding forms of the L and R matrices become

$$L = \begin{pmatrix} |\tilde{\gamma}_{\tau}^{\Omega}| - \mu_f|\tilde{\gamma}_{n}^{\Omega}| & |\tilde{\gamma}_{\tau,+}^{\Gamma}| - \mu_f|\tilde{\gamma}_{n,+}^{\Gamma}| & |\tilde{\gamma}_{\tau,-}^{\Gamma}| - \mu_f|\tilde{\gamma}_{n,-}^{\Gamma}| \\ 0 & I & -I \end{pmatrix}, R = \begin{pmatrix} 0 \\ 0 \end{pmatrix}. \qquad (22)$$

This system is different than the previous sets of equations. The first row in $\boldsymbol{L}$ includes nonlinear relations constructed by Eq. 8, and the second row ensures the continuity of normal displacements across the fracture surfaces, i.e., the physical contact between two fracture surfaces. The subscripts τ and n denote the shear and normal directions of the fracture faces, respectively.

In this study, we use Newton's method [32] to solve the nonlinear system of equations.

4. NUMERICAL SIMULATIONS

The performance of the method is verified with several comparison studies for 2D and 3D domains. We start by examining the convergence properties of the method with a 2D domain that contains only one fracture, located approximately at the middle. Moreover, an example that includes a complicated fracture distribution is also presented to show the capabilities of the method. Finally, the convergence of the method for a 3D case is examined. In this case, we analyse the convergence of the method relative to an approximate reference solution, which is found by a finite-element discretization of the problem. For simplicity, both Lamé parameters of the medium are set to 1 in all numerical simulations.

The convergence of the proposed method is examined by calculating the discrete L2-norm of the displacement,

$$err_{\boldsymbol{u}} = \frac{\left(\sum_{\Omega_i} m_{\Omega_i} \left(\boldsymbol{u}_{ref} - \boldsymbol{u}\right)^2\right)^{\frac{1}{2}}}{\left(\sum_{\Omega_i} m_{\Omega_i} \left(\boldsymbol{u}_{ref}\right)^2\right)^{\frac{1}{2}}}, \tag{23}$$

where m_{Ω_i} is the area of the considered cell and $\boldsymbol{u}_{ref}$ is the reference solution. The traction error is also calculated in a similar manner as
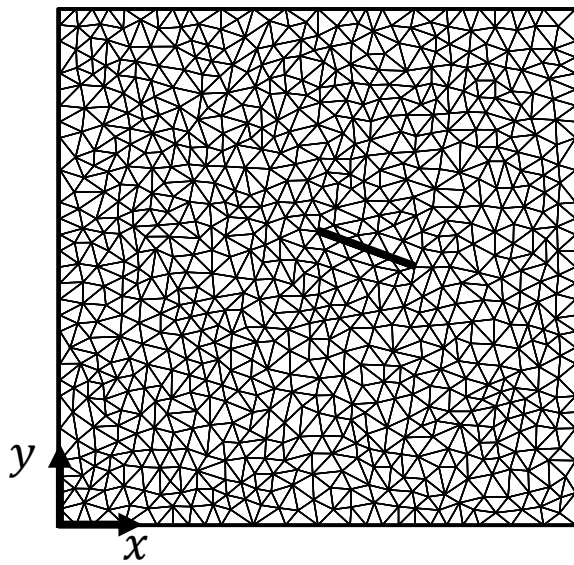
$$err_{\boldsymbol{T}} = \frac{\left(\sum_{\mathcal{F}_{\Omega_i}} m_{\mathcal{F}_{\Omega_i}} \left(\boldsymbol{T}_{ref} - \boldsymbol{T}\right)^2\right)^{\frac{1}{2}}}{\left(\sum_{\mathcal{F}_{\Omega_i}} m_{\mathcal{F}_{\Omega_i}} \left(\boldsymbol{T}_{ref}\right)^2\right)^{\frac{1}{2}}}, \tag{24}$$

where $m_{\mathcal{F}_{\Omega_i}}$ is the area of the considered face and $\boldsymbol{T}_{ref}$ is the reference solution.
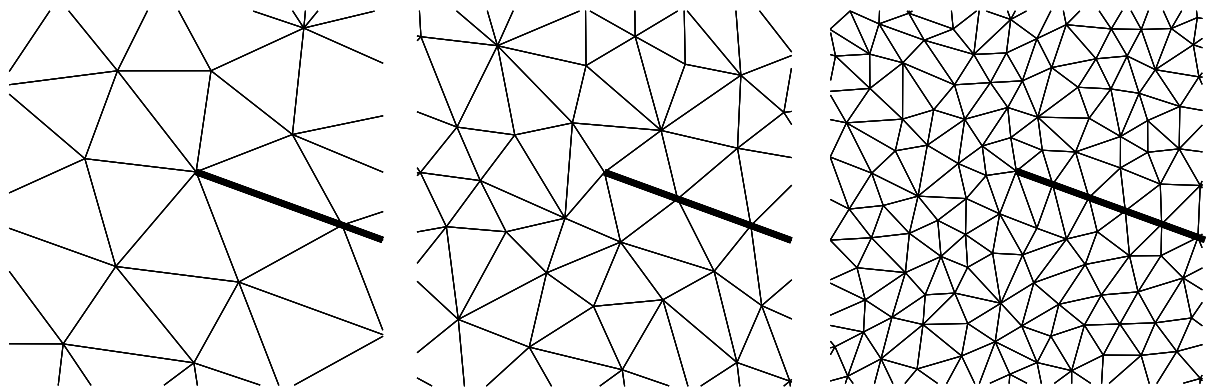
4.1. Validation for Single-Fracture Case

In this part, the validation examples for the three types of problems will be addressed: defined displacement jump at the fracture surfaces (case 1), defined traction at the fracture surfaces (case 2), and fractures controlled by a friction model (case 3). The analytical solutions for each type of problem are available in the literature. However, the analytical solutions are defined in an infinite domain. Therefore, there are limitations in using analytical solutions as reference solutions to examine the convergence properties of the method for the cases in which the boundary effect is significant. In such a case, we use the approximate solution with a very fine grid as the reference solution. The convergence studies for all problems are conducted with the same domain. The total length of the domain is 50 m × 50 m with a fracture located at the centre the domain. The fracture is 10 m in length and is at a 20° angle from the x-axis. The domain is discretized using a non-structured simplex grid. Figure 4 shows an example of the coarsest grid, which has four face pairs to discretize the fracture

surfaces. For convergence studies, refinement of the grid is conducted such that the numbers of face pairs for fracture discretization are 8, 16, 32, 64, and 128. The total number of cells in the domain ranges from approximately 1,500 for the coarsest grid to 1.5 million for the finest. To minimize the dependence on a particular unstructured grid sequence, 10 independent grids were constructed, keeping the number of face pairs constant. Then, the evaluation was extended by calculating the average error for each group of grids with the same number of face pairs. We also used non-hierarchical grid refinement for our analysis. Figure 5 shows an example of the non-hierarchical grid refinement at the same tip area for the first three grid refinements. The refinement is performed depending only on the maximum area of each cell; each time the grid is refined, a new grid is created. We will comment on the effect of non-hierarchical refinement in the results.

Fig. 4 The coarsest grid used for the validation of the method. This example grid is used for the problems that have analytical solutions for single cracks. The thick black line shows the fracture.
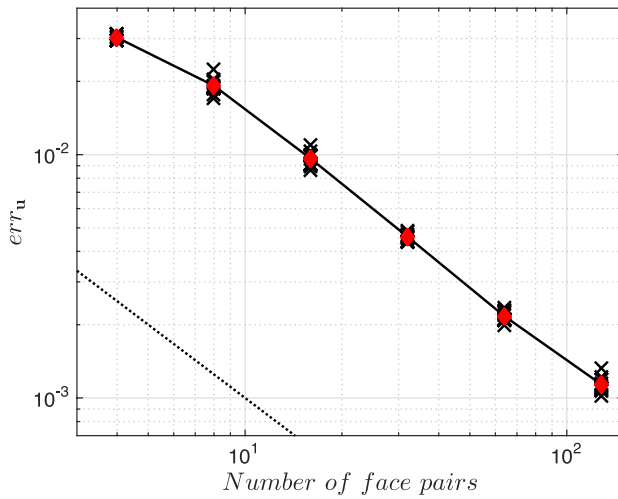

Fig. 5 The non-hierarchical grid refinement shown close to the tip of the fracture. The thin lines show the gridding, while the thick ones represent the fracture. Each time the grid is refined, a new grid is created.

4.1.1. Case 1: Defined Displacement Jump at the Fracture Surfaces
The first validation problem consists of an infinite, two-dimensional, homogeneous, isotropic, elastic, nonporous medium that has a constant displacement discontinuity

over a finite line segment. It is assumed that the displacements are continuous everywhere except the line segment. The line segment is considered a fracture that has positive and negative sides as described in Section 2.2. The constant displacement discontinuity in the tangential direction is defined between the positive and negative sides of the fracture by setting the tangential component of $[\![u]\!]$ in Eq. 6 to 0.001. A detailed description of the problem and the derivation of the analytical solution can be found in [12,13]. The induced displacements and stresses at any point (x, y) in the domain caused by the constant discontinuity are given in the appendix. The traction vectors are calculated for each face using stress values with the face normal vectors.

Figure 6 shows the displacement errors calculated in the whole domain for each grid and the average error. The method is approximately first-order convergent in displacement for this problem, which is lower than in previous numerical studies of MPSA methods without fracture. This behaviour is expected when the domain includes discontinuity. Moreover, since the averages of the displacement errors do not deviate dramatically from the errors calculated for each grid, we can also conclude that the grid structure has only a minor effect on the displacement convergence of the problem.
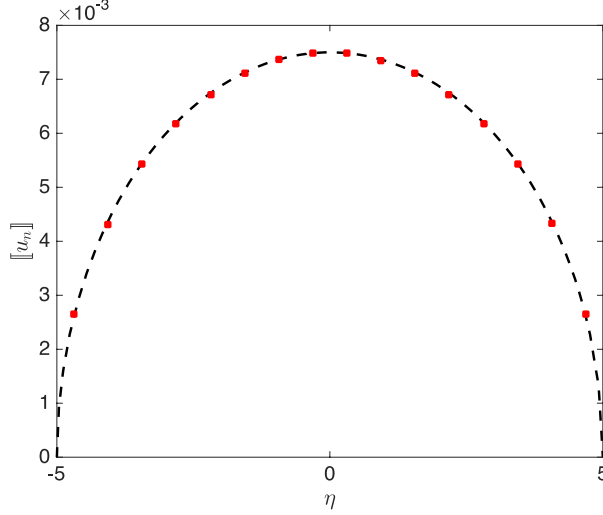

Fig. 6 The convergence behaviour for displacement in the whole domain for case 1. The red diamond shows the average of the error for each group of grids with the same number of face pairs. The dotted line is the 1st-order reference line.

Figure 7 shows the convergence behaviour for stress in the whole domain. As in the previous figure, the line with diamonds in Fig. 7 shows the average values. As we increase the number of DOFs in the domain, the convergence in stress is not observed as expected. This is a common numerical problem associated with the stress values at the tips [33,34]. The errors close to the tip of the fracture are large and oscillatory. Linear elastic fracture-mechanics theory states that the stresses are singular at the tip of the fracture because the gradient of the displacement at the fracture tip is infinite. Therefore, the singularity at the fracture tip affects the convergence severely. When the number of DOFs is increased, the locations of the unknowns approach the singularity at the tip, and the error becomes more dominant. We therefore quantify the stress convergence by following another perspective from Dugdale [35]. As natural materials cannot support infinite stress, this singularity is physically unrealistic. It is known that real materials limit the stress concentrations at crack tips by locally deforming

inelastically. The radius of the inelastic deformation zone at the tip can be estimated by two common approaches: the Dugdale model and the Irwin approach [7]. However, these models depend on the yield strength of the material. For simplicity, the tip zone radius for the current study is considered to be 0.12, which is estimated by taking a much smaller length than the fracture length. When we define the radius for the tip zone and check the convergence behaviour outside the tip zone, the stress convergence is dramatically improved. This effect is shown in Fig. 7 by the line with stars. In addition, since the averages of the stress errors do not deviate dramatically from the errors calculated for each grid, we can again conclude that the grid structure has only a minor effect on the stress convergence of the problem.

Fig. 7 The convergence behaviour for stress in the whole domain for case 1. The line with diamonds shows the average stress convergence behaviour dominated by error caused at the fracture tips, whereas the line with stars shows the stress convergence behaviour when the tips of the fracture are eliminated. The dotted line is the 1st-order reference line.

4.1.2. Case 2: Defined Traction at the Fracture Surfaces

The second validation problem is defined in the same domain as case 1. This time, the fracture is subject to a constant pressure along its surfaces. The constant pressure can be considered as constant traction in the direction normal to the fracture faces. An analytical solution for the opening between the fracture surfaces (i.e., the normal relative displacement between the fracture surfaces) was derived by Sneddon [36] as
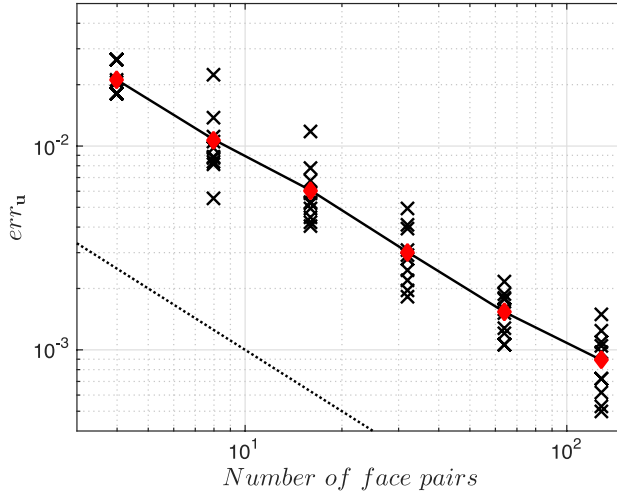
$$\llbracket u_n \rrbracket = \frac{(1-v)P\Delta L}{\mu}\sqrt{1 - \frac{\eta^2}{(\Delta L/2)^2}}, \tag{25}$$

where v is Poisson's ratio, μ is the shear modulus, $P=0.001$ is the applied pressure, ΔL is the fracture length, and $-\Delta L/2 \leq \eta \leq \Delta L/2$. Note that the traction forces are applied to the fracture surfaces only in the normal direction; therefore, while Eq. 25 gives the normal component of the displacement jump, the shear components of the displacement jump are not defined. The comparison between the analytical solution and the solution approximated using 16 face pairs is shown in Fig. 8. The approximate solution is consistent with the analytical solution.

Fig. 8 Comparison between the analytical solution and the solution approximated using 16 face pairs for the pressurized fracture problem (case 2). The dashed line shows the analytical solution, while the red dots show the numerical solution.

Although the approximate solution is consistent with the numerical solution, the grid structure and the singularity of the stress at the fracture tip have dominant effects on the solution since the forces are defined on the fracture faces. This effect can be clearly observed in Fig. 9, where both the error of all grids and their average is shown. Note that we observed smaller deviations from the average value when we used structured grids at the fracture tips. The method provides 1st-order convergence on average in this case as well.

Fig. 9 The average convergence behaviour for displacement at the fracture for case 2. The red diamond shows the average of the error for each group of grids with the same number of face pairs. The dotted line is the 1st-order reference line.

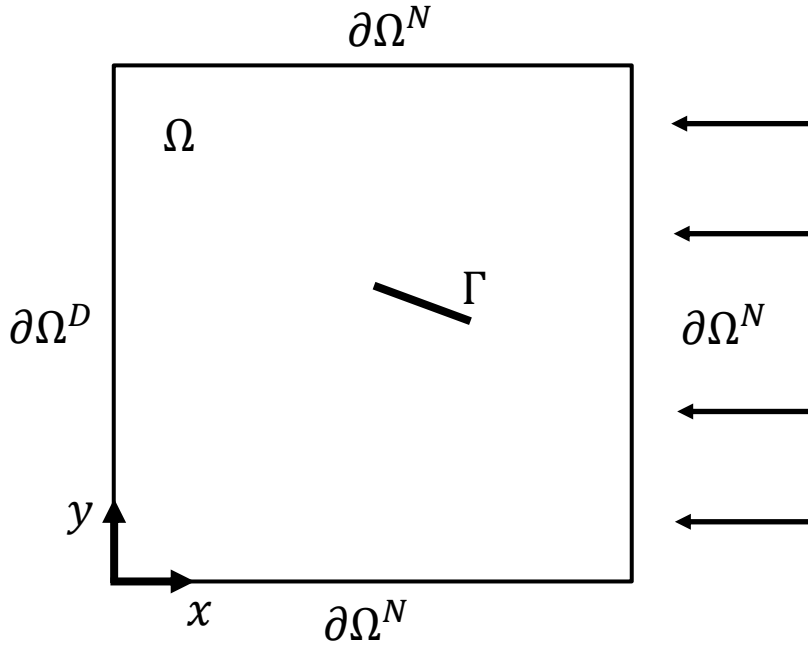### 4.1.3. Case 3: Fractures Controlled by a Friction Model
In this case, the frictional sliding of a single fracture is considered. We use the same computational domain as in cases 1 and 2. The angles of the fracture inclination and the friction are 20° and 30°, respectively. For the current problem, we wish to create boundary conditions such that the fracture is subject to a compressive stress of σ_{xx},

14

while the physical contact between fracture faces is maintained during the simulation. The considered stress conditions can be written as

$$\sigma_{xx} = 0.001, \tag{26}$$
$$\sigma_{yy} = 0,$$
$$\sigma_{xy} = 0.$$

Figure 10 illustrates the boundary conditions for this case. We apply these stress conditions as Neumann boundary conditions on the boundary $\partial\Omega^N$. To avoid an indefinite problem, we define a Dirichlet boundary condition on one side of the domain, $\partial\Omega^D$. For $\partial\Omega^D$, the displacement at the origin and in the x-direction, u_x, is set to zero, and the displacement in the y-direction, u_y, is found with the help of Hooke's law, 2D strain-displacement relations, and Eq. 26 as

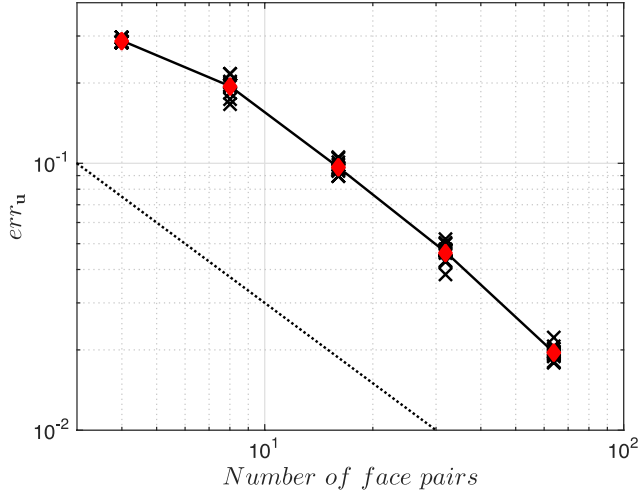$$\sigma_{yy} = \lambda\varepsilon_{xx} + (\lambda + 2\mu)\varepsilon_{yy} \text{ where } \varepsilon_{xx} = \frac{\partial u_x}{\partial x}, \varepsilon_{yy} = \frac{\partial u_y}{\partial y}, \tag{27}$$

$$\frac{\partial u_x}{\partial x} = -\frac{(\lambda + 2\mu)}{\lambda}\frac{\partial u_y}{\partial y},$$

$$\sigma_{xx} = \lambda\varepsilon_{yy} + (\lambda + 2\mu)\varepsilon_{xx},$$

$$\frac{\partial u_y}{\partial y} = \frac{0.001}{-\frac{(\lambda + 2\mu)(\lambda + 2\mu)}{\lambda} + \lambda}.$$

Fig. 10 Boundary conditions used for the case in which the fracture deformation is controlled by a friction model. The fracture is under compressive stress.

In this problem, the convergence of the numerical solution is examined using the solution with the finest grid as the reference solution. The convergence rate for the displacement is shown in Fig. 11. As in the previous cases, the average convergence is of 1st order. Moreover, the averages of the displacement errors exhibit only minor deviation from the errors calculated for each grid.

Fig. 11 The convergence behaviour for displacement at the fracture for the nonlinear problem. The red diamond shows the average of the error for each group of grids with the same number of face pairs. The dotted line is the 1st-order reference line.
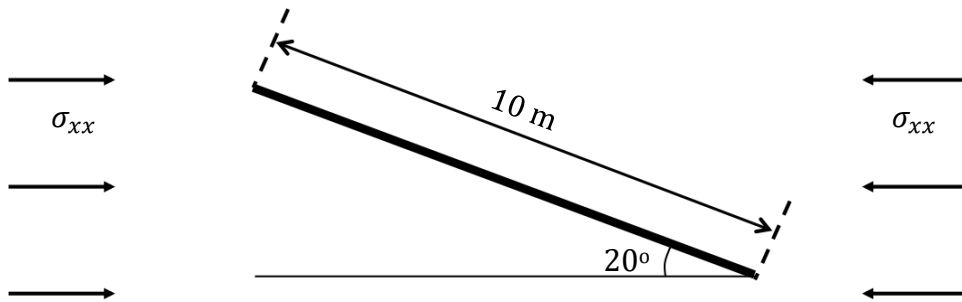
In addition to the convergence analysis shown in Fig 11, we also make a qualitative comparison between an existing analytical solution for the problem defined in an unbounded domain and the approximate solution defined in a bounded domain. Figure 12 illustrates the geometrical configuration of the analytical problem. The analytical solutions for the shear component of the displacement jump between fracture surfaces are given in [37] as

$$T_n = -\sigma_{xx} \sin^2 \alpha, \tag{28}$$

$$[\![u_\tau]\!] = \frac{4(1-v^2)T_\tau}{E} \sqrt{\left(\frac{\Delta L}{2}\right)^2 - \left(\eta - \frac{\Delta L}{2}\right)^2},$$
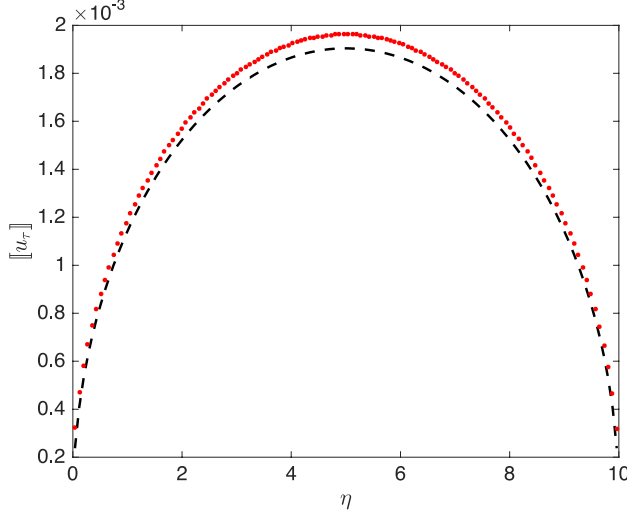
$$T_\tau = \sigma_{xx} \sin \alpha \left(\cos \alpha - \sin \alpha \tan \phi\right),$$

where $0 \leq \eta \leq \Delta L$, T_n is the normal traction, T_τ is the shear traction, α is the fracture inclination angle, ϕ is the friction angle, and E is Young's modulus.

Fig. 12 A crack under compression in an unbounded domain.

Figure 13 shows the analytical solution and the numerical solution of the shear displacement between the fracture surfaces. As expected, there is only a small difference between the analytical and numerical solutions. The main reason for the difference between the two solutions is the discrepancy between boundary conditions. The number of iterations of the nonlinear solver is 2 for this problem.
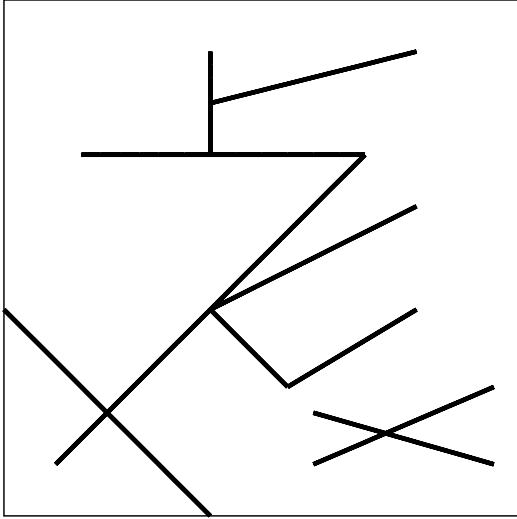
Fig. 13 The shear displacement controlled by friction. The analytical solution is shown as a dashed line, whereas the numerical solution is shown as red dots. For this numerical solution, 124 face pairs are used.
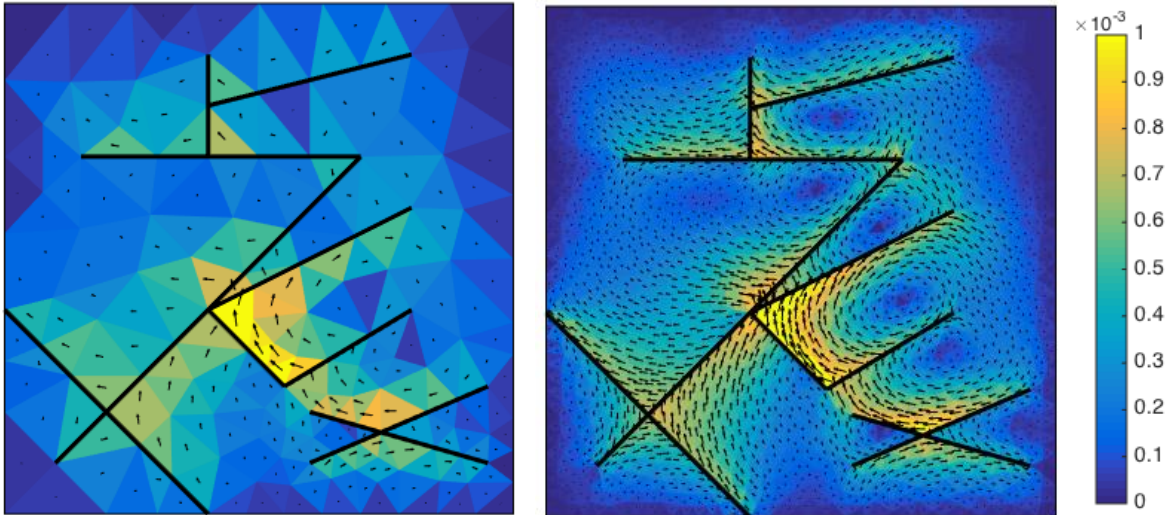
4.2. More Complex Numerical Examples

We now consider more complex fracture geometries. We first examine the convergence properties of the method when the domain includes several complications in the numerical sense. Then, we examine a 3D domain with a fracture in the middle. We also show the convergence behaviour for the 3D example, based on a reference solution that is approximated using the finite-element method.

4.2.1. Numerical Example with Intersecting Fractures

After the validation of the method illustrated in Section 4.1, a more challenging domain, shown in Fig. 14, is examined to demonstrate the capabilities of the method. The domain is discretized using a non-structured simplex grid. The domain includes challenges such as fracture intersections of several types, a fracture passing through the domain, and a disconnected fracture network. These numerical challenges are handled straightforwardly by the model as the variables for the fracture faces are defined at the centres of the grid faces, as described in Section 3. In addition, the method can accommodate fractures that have immersed tips and fractures that cross the boundary, if the grid is created accordingly (see Section 3.1). Here, we prescribe a constant displacement jump between fracture faces. The displacement is defined in the shear direction of each fracture. Figure 15 shows the deformation results for two grids with 47 and 160 face pairs to discretize the fractures. The colours indicate the magnitudes of the deformations, and the directions of the deformations are shown with arrows. The sizes of the arrows are also related to the deformation magnitudes. The results from using the coarse and fine meshes are consistent.
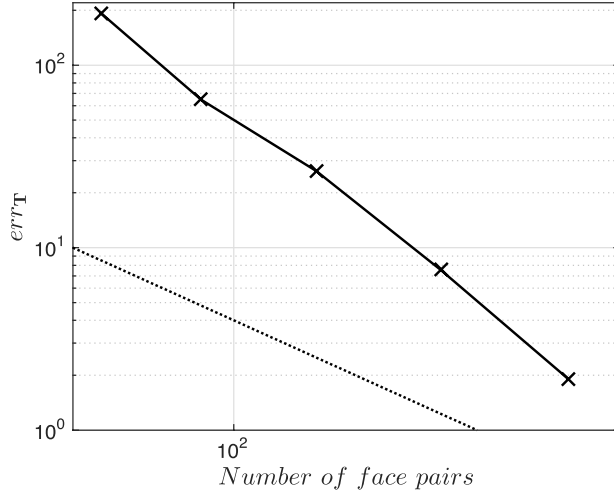
Fig. 14 The domain includes several intersections as intersecting fractures and disconnected fracture networks.

Fig. 15 Approximate deformation distributions for the solution using 47 face pairs to discretize the fractures (left) and the solution using 160 face pairs to discretize the fractures (right).

To conduct a convergence examination for this example, the reference solution is obtained using a relatively fine grid with 1,300 face pairs to discretize the fractures. The convergence study is performed by comparing the tractions at the fracture faces between solutions obtained using coarser grids and the reference solution. Figure 16 shows the convergence ratio of the problem. The convergence ratio for this problem is higher than 1st order.
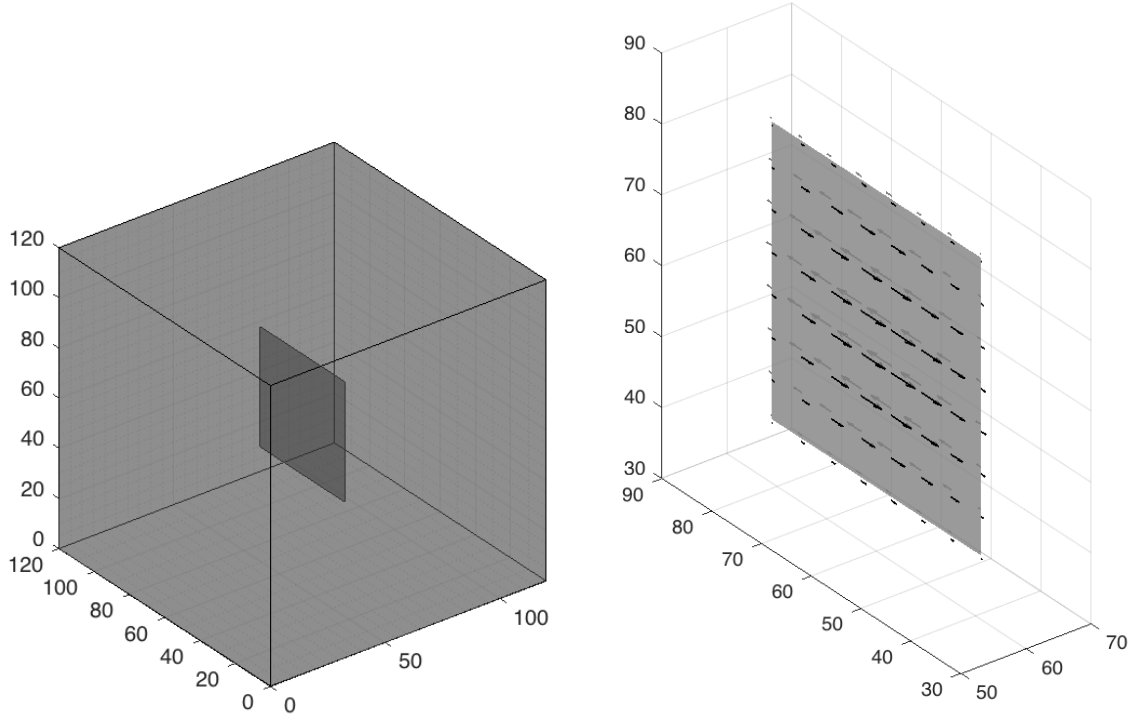
Fig. 16 The convergence behaviour for the problem includes several numerical challenges. The dotted line is the 1st-order reference line.

4.2.2. Comparison Example with Finite-Element Method (3D)

As a final example, we examined a 3D domain with a fracture in the middle. The domain is discretized using a structured hexahedron grid. A lateral displacement jump at the fracture surfaces is defined. The domain and the defined jump are shown in Fig. 17. The displacement jump is defined such that its maximum value is attained at the middle of the fracture and is zero at the edges of the fracture. The equation defining the lateral component of the jump can be written as
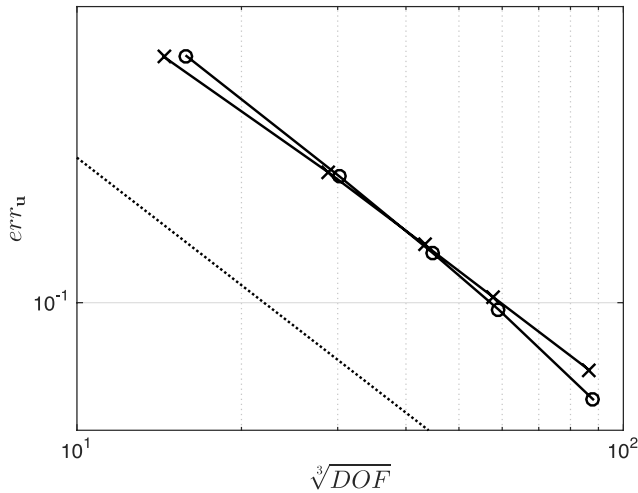
$$[\![u_\tau]\!] = 0.001 \left(\sin\left(\frac{\pi \eta_x}{\Delta L}\right) \sin\left(\frac{\pi \eta_y}{\Delta L}\right) \right). \tag{29}$$

The length of each edge of the fracture, ΔL, is 36, and η_x and η_y are the local coordinates relative to the fracture.

Fig. 17 The considered 3D domain with a fracture (left). The fracture is shown in dark grey in the middle. Distribution of the prescribed jump at the fracture faces (right).

The reference solution for this problem was obtained by finite-element discretization using a relatively fine grid. We used the open-source software package Pylith [16,38], which was developed for the simulation of crustal deformations. Similar to the current method, Pylith uses cohesive cells and adds DOFs to the grid to define the relative motion of the fracture surfaces. Figure 18 shows the convergence for displacement for both the current method and FEM (Pylith). The convergence ratio is slightly higher than 1 for FEM (Pylith) and slightly lower than 1 for MPSA. The improved convergence order of the finite-element method may be related to the reference solution being calculated with this method.

Fig. 18 Convergence behaviour for displacement in the 3D problem. The line with circles shows the Pylith (FEM) results, and the line with crosses shows the MPSA results. The dotted line is the 1st-order reference line.

5. CONCLUSION

Motivated by the modelling of subsurface applications, an FVM for the deformation of fractured media, in which pre-existing fractures are represented explicitly in the model, was proposed. The method was constructed based on MPSA with the same grid structure as the FVM for flow, e.g., multi-point flow approximations. The method is therefore particularly well suited for problems involving coupled flow and deformation in fractured formations.

The fractures in a medium physically represent internal discontinuities, and the physics of processes related to fractures can differ and can be modelled by different governing equations than those of the rest of the medium. We considered three models for the deformation of the fractures coupled to the rest of the medium: (1) defined displacement jump at the fracture surfaces, (2) defined traction at the fracture surfaces, and (3) a friction model controlling the fracture behaviour more specifically. Our approach treats fractures as internal boundary conditions, which naturally allows for different deformation models for the fractured and non-fractured media. The internal boundary conditions that represent fracture surfaces are considered as line pairs (for 2D) or faces (for 3D), and the required equations for the fracture behaviour are defined between pairs.

To verify the model, the convergence of the method was examined for several benchmark problems. Although the lack of special treatment for the singularity at the fracture tip decreases the convergence rate, we have shown that the method has approximately 1st-order convergence in displacement for all the cases that we examined.

The approach results in a method with a broad application area. Numerical examples demonstrate the flexibility of the method by considering different models for fracture deformation.
We have also shown that the method can handle complicated fracture networks and 3D cases. Considering its advantages in the coupling of fluid flow and mechanical deformation, the method is well suited for the further development of simulation tools for a wide range of subsurface engineering applications.

Acknowledgements

APPENDIX

The analytical solutions of the induced displacements, u_x, u_y, and stresses, σ_{xx}, σ_{yy}, σ_{xy}, at any point (x, y) for an infinite two-dimensional homogeneous and isotropic elastic nonporous medium containing a finite small thin fracture with constant normal- and shear-displacement discontinuities are given by Crouch and Starfield [12] as

$$u_x = [\![u_n]\!]\left(2(1-v)\frac{\partial f}{\partial y} - y\frac{\partial^2 f}{\partial x^2}\right) + [\![u_\tau]\!]\left(-(1-2v)\frac{\partial f}{\partial x} - y\frac{\partial^2 f}{\partial x \partial y}\right), \qquad (30)$$

$$u_y = [\![u_n]\!]\left((1-2v)\frac{\partial f}{\partial x} - y\frac{\partial^2 f}{\partial x \partial y}\right) + [\![u_\tau]\!]\left(2(1-v)\frac{\partial f}{\partial y} - y\frac{\partial^2 f}{\partial y^2}\right),$$

and

$$\sigma_{xx} = 2\mu[\![u_n]\!]\left(2\frac{\partial^2 f}{\partial x \partial y} + y\frac{\partial^3 f}{\partial x \partial y^2}\right) + 2\mu[\![u_\tau]\!]\left(\frac{\partial^2 f}{\partial y^2} + y\frac{\partial^3 f}{\partial y^3}\right),$$

$$\sigma_{yy} = 2\mu[\![u_n]\!]\left(-y\frac{\partial^3 f}{\partial x \partial y^2}\right) + 2\mu[\![u_\tau]\!]\left(\frac{\partial^2 f}{\partial y^2} - y\frac{\partial^3 f}{\partial y^3}\right),$$

$$\sigma_{xy} = 2\mu[\![u_n]\!]\left(\frac{\partial^2 f}{\partial y^2} + y\frac{\partial^3 f}{\partial y^3}\right) + 2\mu[\![u_\tau]\!]\left(-y\frac{\partial^3 f}{\partial x \partial y^2}\right),$$

(31)

where $[\![u_n]\!]$ and $[\![u_\tau]\!]$ are the displacement discontinuities in the normal and shear directions, respectively, μ is the shear modulus, v is Poisson's ratio, and f is a function of the position (x, y) of the field point relative to the centre of the fracture. Denoting the half radius of the fracture as a, f is given as

$$f(x, y) = -\frac{1}{4\pi(1-v)}\left(y\left(\tan^{-1}\frac{y}{x-a} - \tan^{-1}\frac{y}{x+a}\right)\right)$$

$$-(x-a)\ln\sqrt{(x-a)^2 + y^2} + (x+a)\ln\sqrt{(x+a)^2 + y^2}.$$

(32)

REFERENCES

1. Jaeger, J.C., Cook, N.G., Zimmerman, R.: Fundamentals of rock mechanics. John Wiley & Sons, (2009)
2. Jing, L.: A review of techniques, advances and outstanding issues in numerical modelling for rock mechanics and rock engineering. Int. J. Rock Mech. Min. **40**(3), 283-353 (2003). doi:10.1016/s1365-1609(03)00013-3
3. McClure, M.W., Horne, R.N.: An investigation of stimulation mechanisms in Enhanced Geothermal Systems. Int. J. Rock Mech. Min. **72**, 242-260 (2014). doi:10.1016/j.ijrmms.2014.07.011
4. Oldenburg, C., Pruess, K., Benson, S.M.: Process modeling of CO2 injection into natural gas reservoirs for carbon sequestration and enhanced gas recovery. Energ. Fuel. **15**(2), 293-298 (2001).
5. Rutqvist, J.: Status of the TOUGH-FLAC simulator and recent applications related to coupled fluid flow and crustal deformations. Comput. Geosci. **37**(6), 739-750 (2011). doi:10.1016/j.cageo.2010.08.006
6. Rutqvist, J., Stephansson, O.: The role of hydromechanical coupling in fractured rock engineering. Hydrogeol. J. **11**(1), 7-40 (2003). doi:10.1007/s10040-002-0241-5
7. Anderson, T.L.: Fracture mechanics: fundamentals and applications. CRC press, (2005)
8. Adachi, J., Siebrits, E., Peirce, A., Desroches, J.: Computer simulation of hydraulic fractures. Int. J. Rock Mech. Min. **44**(5), 739-757 (2007). doi:10.1016/j.ijrmms.2006.11.006
9. Liu, Y.J., Mukherjee, S., Nishimura, N., Schanz, M., Ye, W., Sutradhar, A., Pan, E., Dumont, N.A., Frangi, A., Saez, A.: Recent Advances and Emerging Applications of the Boundary Element Method. Appl. Mech. Re. **64**(3), 030802 (2012). doi:10.1115/1.4005491
10. McClure, M.W., Horne, R.N.: Investigation of injection-induced seismicity using a coupled fluid flow and rate/state friction model. Geophysics **76**(6), WC181-WC198 (2011). doi:10.1190/geo2011-0064.1

11. Norbeck, J.H., McClure, M.W., Lo, J.W., Horne, R.N.: An embedded fracture modeling framework for simulation of hydraulic fracturing and shear stimulation. Computat. Geosci. **20**(1), 1-18 (2016).
12. Crouch, S.L., Starfield, A.: Boundary element methods in solid mechanics: with applications in rock mechanics and geological engineering. Allen & Unwin, (1982)
13. Shou, K., Crouch, S.: A higher order displacement discontinuity method for analysis of crack problems. In: International journal of rock mechanics and mining sciences & geomechanics abstracts 1995, vol. 1, pp. 49-55. Elsevier
14. Zhou, X., Ghassemi, A.: Three-dimensional poroelastic analysis of a pressurized natural fracture. Int. J. Rock Mech. Min. **48**(4), 527-534 (2011). doi:10.1016/j.ijrmms.2011.02.002
15. Borja, R.I.: Plasticity. Springer, (2013)
16. Aagaard, B.T., Knepley, M.G., Williams, C.A.: A domain decomposition approach to implementing fault slip in finite-element models of quasi-static and dynamic crustal deformation. J. Geophys. Res.-Sol. Ea. **118**(6), 3059-3079 (2013). doi:10.1002/jgrb.50217
17. Kuna, M.: Finite elements in fracture mechanics. Springer, (2013)
18. Garipov, T.T., Karimi-Fard, M., Tchelepi, H.A.: Discrete fracture model for coupled flow and geomechanics. Computat. Geosci. **20**(1), 149-160 (2016). doi:10.1007/s10596-015-9554-z
19. Kim, J., Tchelepi, H.A., Juanes, R.: Stability and convergence of sequential methods for coupled flow and geomechanics: Fixed-stress and fixed-strain splits. Comput. Methpd. Appl. M. **200**(13-16), 1591-1606 (2011). doi:10.1016/j.cma.2010.12.022
20. Kim, J., Tchelepi, H.A., Juanes, R.: Stability, accuracy and efficiency of sequential methods for coupled flow and geomechanics. In: SPE reservoir simulation symposium 2009. Society of Petroleum Engineers
21. Castelletto, N., White, J.A., Tchelepi, H.A.: Accuracy and convergence properties of the fixed-stress iterative solution of two-way coupled poromechanics. Int. J. Numer. Anal. Met. **39**(14), 1593-1618 (2015). doi:10.1002/nag.2400
22. Nordbotten, J.M.: Cell-centered finite volume discretizations for deformable porous media. Int. J. Numer. Meth. Eng. **100**(6), 399-418 (2014). doi:10.1002/nme.4734
23. Nordbotten, J.M.: Stable Cell-Centered Finite Volume Discretization for Biot Equations. Siam. J. Numer. Ana. **54**(2), 942-968 (2016). doi:10.1137/15m1014280
24. Keilegavlen, E., Nordbotten, J.M.: Finite volume methods for elasticity with weak symmetry. arXiv preprint arXiv:1512.01042 (2015).
25. Andrews, D.: Test of two methods for faulting in finite-difference calculations. Bull. Seismol. Soc. Am. **89**(4), 931-937 (1999).
26. Rahman, M., Hossain, M., Rahman, S.: A shear - dilation - based model for evaluation of hydraulically stimulated naturally fractured reservoirs. Int. J. Numer. Anal. Met. **26**(5), 469-497 (2002).
27. Daub, E.G., Carlson, J.M.: Friction, fracture, and earthquakes. Annu. Rev. Condens. Matter Phys. **1**(1), 397-418 (2010).
28. Kloosterman, G.: Contact methods in finite element simulations. University of Twente, (2002)
29. Ida, Y.: Cohesive force across the tip of a longitudinal - shear crack and Griffith's specific surface energy. J. Geophys. Res. **77**(20), 3796-3805 (1972).

30. Andrews, D.: Rupture models with dynamically determined breakdown displacement. Bull. Seismol. Soc. Am. **94**(3), 769-775 (2004).
31. Dieterich, J.H.: Modeling of rock friction: 1. Experimental results and constitutive equations. J. Geophys. Res. **84**(B5), 2161 (1979). doi:10.1029/JB084iB05p02161
32. Kelley, C.T.: Solving nonlinear equations with Newton's method, vol. 1. Siam, (2003)
33. Zehnder, A.T.: Fracture Mechanics. Lecture Notes in Applied and Computational Mechanics, vol. 62. Springer Netherlands, (2012)
34. Lawn, B.: Fracture of brittle solids. Cambridge university press, (1993)
35. Dugdale, D.S.: Yielding of steel sheets containing slits. J. Mech. Phys. Solids **8**(2), 100-104 (1960).
36. Sneddon, I.N., Transforms, F.: McGraw Hill Book Co. Inc., New York (1951).
37. Phan, A.V., Napier, J.A.L., Gray, L.J., Kaplan, T.: Symmetric-Galerkin BEM simulation of fracture with frictional contact. Int. J. Numer. Meth. Eng. **57**(6), 835-851 (2003). doi:10.1002/nme.707
38. Aagaard, B., Knepley, M., Williams, C., Strand, L., Kientz, S.: PyLith user manual, version 2.1.0. Comput. Infrastruct. Geodyn. (2015).